Mechanistic Insights into the Structure-Dependent Selectivity of Catalytic Furfural Conversion on Platinum Catalysts

Qiu-Xia Cai and Jian-Guo Wang
College of Chemical Engineering, Zhejiang University of Technology, Hangzhou 310014, China

Yang-Gang Wang and Donghai Mei
Fundamental and Computational Sciences Directorate and Institute for Integrated Catalysis, Pacific Northwest National Laboratory, Richland, WA 99352

DOI 10.1002/aic.14902
Published online June 24, 2015 in Wiley Online Library (wileyonlinelibrary.com)

The effects of surface structures on the selectivity of catalytic furfural conversion over platinum (Pt) catalysts in the presence of hydrogen have been studied using first principles density functional theory (DFT) calculations and microkinetic modeling. Three Pt model surface structures, that is, flat Pt(111), stepped Pt(211), and Pt_{55} cluster are chosen to represent the terrace, step, and corner sites of Pt nanoparticle. DFT results show that the dominant reaction route (hydrogenation or decarbonylation) in furfural conversion depends strongly on the structures (or reactive sites). Using the size-dependent site distribution rule, our microkinetic modeling results indicate the decarbonylation route prevails over smaller Pt particles less than 1.4 nm while the hydrogenation is the dominant reaction route over larger Pt catalyst particles at $T = 473$ K and $P_{H_2} = 93$ kPa. This is in good agreement with the reported experimental observations. © 2015 American Institute of Chemical Engineers *AIChE J*, 61: 3812–3824, 2015
Keywords: catalysis, biomass conversion, structure-dependent selectivity, density functional theory, microkinetic modeling

Introduction

The production of transportation fuels and valuable chemicals from renewable biomass resources is of great interests due to the increasing environmental concerns and energy demand.[1–3] To increase the energy density and stability,[2–6] the bio-oils that are generated by fast pyrolysis or liquefaction of lignocellulosic biomass, need to be upgraded to remove the oxygen via catalytic hydrodeoxygenation (HDO) processes. Furfural is one of major compounds in bio-oils.[7,8] Therefore, catalytic conversion of furfural in the presence of hydrogen using supported transition metal catalysts has been extensively studied as one of the model HDO reactions in the bio-oil upgrading.[7,9–20] Although various products could be obtained using different catalysts under experimental conditions which recently reviewed,[19,21] there are two major reaction routes in the furfural HDO conversion.[10,11,13] As shown in Figure 1, the first reaction route is the furfural hydrogenation where the carbonyl group of furfural is hydrogenated leading to furfuryl alcohol. In the second decarbonylation route, the C_4—C_5 bond of furfural is cleaved leading to the formation of furan. Previous experimental studies[10–15] suggested that the two major reaction routes were competitive. The selectivities of hydrogenation and decarbonylation are not only dependent on reaction conditions such as temperature and hydrogen partial pressure but also controlled by the nature and dispersion of supported metal catalysts.[13–17] For example, Sitthisa et al. found that the hydrogenation prevails at low temperatures while decarbonylation becomes significant at high temperatures over Ni/SiO_2.[14] Sitthisa and Resasco compared the selectivity of furfural conversion over silica supported Cu, Pd, and Ni catalysts at 230°C.[13] They found that furfuryl alcohol is the major product with the selectivity of over 98% on Cu/SiO_2 while the selectivity to furan reaches up to 60% on Pd/SiO_2 and 43% on Ni/SiO_2. They attributed the distinguished selectivity difference to the different adsorbed configurations of furfural and subsequent reaction intermediates on three metal surfaces. Pushkarev et al. studied catalytic furfural conversion over a series of mesoporous silica supported Pt catalysts.[11] They found that the product selectivity is largely dependent upon the particle size and shape. Furfural decarbonylation is the dominant reaction route over smaller Pt nanoparticles (<2.5 nm) while furfural hydrogenation prevails over larger Pt nanoparticles. The effects of the particle size and active site on the selectivity of furfural conversion were observed over supported Pd catalysts.[10] Using alkanethiolate self-assembled monolayers as the modifier that controls the availability of specific active sites on the supported Pd catalysts, Pang et al. concluded that furfural hydrogenation occurs primarily on the step edges or the defect sites while decarbonylation most likely occurs on the terrace sites.[10] All these experimental evidence indicates that catalytic furfural conversion on supported metal catalysts is a structure sensitive reaction.

Additional Supporting Information may be found in the online version of this article.

Correspondence concerning this article should be addressed to J. G. Wang at jgw@zjut.edu.cn or D. Mei at donghai.mei@pnnl.gov.

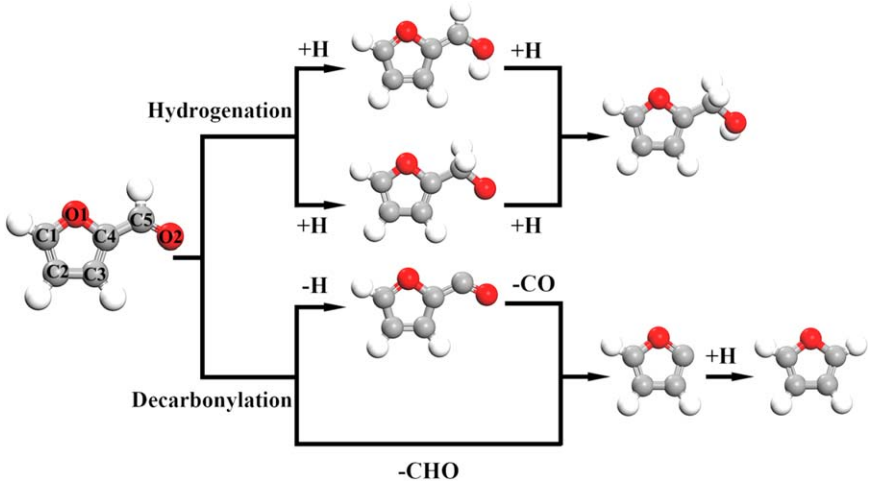

Figure 1. Reaction scheme for furfural conversion in the presence of hydrogen.

[Color figure can be viewed in the online issue, which is available at wileyonlinelibrary.com.]

First principles-based density functional theory (DFT) calculations have been proved a powerful tool to explain the experimental results and more importantly to obtain the mechanistic insight into the heterogeneous catalytic reactions over solid catalysts.[22,23] Sitthisa and Resasco found that furfural most likely adsorbs on the Cu surface through η^1(O) configuration with a single Cu—O bond while furfural binds with Pd and Ni surfaces in the η^2-(C,O) configuration where both C and O atoms of the carbonyl group bind with the surface metal atoms.[13] In the η^1(O) configuration, the strong repulsive interaction between the furanic ring and surface inhibits its C—C bond scission. Therefore, the hydrogenation of the carbonyl group of furfural generating furfuryl alcohol is favored.[14] Similarly, due to the strong interaction between the oxyphilic Fe atom and the carbonyl oxygen atom, the addition of Fe onto the Ni catalyst causes the η^1(O) configuration of furfural promotes the selectivity of hydrogenation.[12] On the basis of comprehensive DFT calculations of reaction energies and activation barriers for all possible elementary steps involving in the hydrogenation and decarbonylation on Pd(111), Vorotnikov et al. concluded that the decarbonylation of the adsorbed furfural to furan and CO is thermodynamically favored although the hydrogenation into furfuryl alcohol is slightly kinetically favorable on Pd(111).[24]

It has been well known that the activity and selectivity of many structure sensitive catalytic reactions can be optimized by changing the size and shape of supported metal catalysts.[23,25–27] Inspired by reported experimental work of furfural HDO over supported Pt catalysts,[11] we investigated the effect of surface structure on the selectivity of furfural HDO over Pt catalysts. Unlike the previous theoretical modeling of furfural reaction using DFT calculations in which only flat (111) structure was investigated, three model Pt surfaces, that is, periodic Pt(111) and Pt(211) surfaces, as well as Pt_{55} cluster were used. These model surfaces were chosen to represent the terrace, step, and corner sites of supported Pt nanoparticles. In this way, the site-specific selectivity of furfural transformation in the presence of hydrogen was explored. With the assumption of the size-dependent site distribution rule, we correlated site distributions as a function of Pt particle size. By combining DFT calculations with microkinetic modeling, we studied the effect of particle size on the selectivity of furfural conversion under experimental reaction conditions. Our modeling results not only agree well with reported experimental results but also provide the fundamental insights into the furfural conversion on metal catalysts at the molecular level.

Methods

At present, it is still a computational challenge to directly simulate the catalytic properties over different sizes of metal nanoparticles. Therefore, a simple method to describe the relationship between the Pt particle size and catalytic properties is developed. The following steps are necessary.

1. The periodic Pt(111) and Pt(211) surfaces, as well as a small metal Pt_{55} nanocluster were chosen to represent the terrace, step, and corner sites of supported Pt nanoparticles. The adsorption of reactants and products, as well as the reaction energetics of elementary steps are calculated from DFT.
2. The microkinetic modeling is used to describe the relationship between the catalytic properties (selectivity) and the reaction sites (terrace, step, and corner).
3. According to the distribution fractions of reaction sites over an ideal polyhedral metal nanoparticle and the results of step (2), the selectivity of Pt nanoparticles of various sizes are predicted.

Density functional theory

All DFT calculations were performed using the Vienna *ab initio* simulation package (VASP).[28–30] The core and valence electrons were represented by the projector augmented wave method with a kinetic cutoff energy of 400 eV.[31,32] The generalized gradient approximation (GGA) combined with the Perdew–Burke–Ernzerhof functional[33] describing the exchange correlation functional was used in the calculations. The van der Waals (vdW) interactions in the VASP code were implemented via a self-consistent vdW-DF functional.[34,35] The ground-state atomic geometries of clean and adsorbed systems were obtained by minimizing the forces on each atom to below 0.05 eV/Å.

Three Pt model surfaces were studied in the present work. The periodic flat Pt(111) and stepped Pt(211) surfaces with the (3×3) and the (1×4) supercell and four atomic layers were used to represent the terrace and step sites of Pt nanoparticles. During the optimization, the adsorbate(s) and the metal atoms of the top two surface layers were allowed to relax while the

Table 1. DFT-Based Kinetic Parameters for Furfural Hydrogenation and Decarbonylation on Pt(111), Pt(211), and Pt_{55} Used in the Microkinetic Modeling

Step	Elementary Reactions	Pt(111)		Pt(211)		Pt_{55}	
		A_i (s^{-1}) (A_{-i})	E_{ai} (eV) (E_{a-i})	A_i (s^{-1}) (A_{-i})	E_{ai} (eV) (E_{a-i})	A_i (s^{-1}) (A_{-i})	E_{ai} (eV) (E_{a-i})
	Hydrogenation						
R1	$C_4H_3(CHO)O(g) + * \leftrightarrow C_4H_3(CHO)O*$	1.0×10^{-5} (4.4×10^{15})	0.00 (1.36)	1.0×10^{-5} (3.1×10^{15})	0.00 (1.95)	1.0×10^{-5} (8.2×10^{13})	0.00 (2.32)
R2	$H_2(g) + 2* \leftrightarrow 2H*$	0.02 (6.2×10^{17})	0.00 (0.61)	0.02 (2.6×10^{17})	0.00 (0.73)	0.02 (1.6×10^{18})	0.00 (2.18)
R3	$C_4H_3(CHO)O* + H* \leftrightarrow C_4H_3(CHOH)O* + *$	1.4×10^{13} (3.2×10^{13})	0.34 (0.17)	9.5×10^{12} (2.3×10^{13})	0.40 (0.04)	1.2×10^{13} (4.9×10^{13})	0.84 (0.30)
R4	$C_4H_3(CHOH)O* + H* \leftrightarrow C_4H_3(CH_2OH)O* + *$	9.7×10^{12} (1.8×10^{14})	0.34 (0.79)	3.2×10^{12} (5.4×10^{13})	0.36 (0.67)	6.4×10^{11} (3.1×10^{13})	0.65 (0.71)
R5	$C_4H_3(CHO)O* + H* \leftrightarrow C_4H_3(CH_2O)O* + *$	1.8×10^{12} (8.4×10^{13})	0.71 (0.34)	1.1×10^{12} (3.8×10^{13})	0.54 (0.39)	2.7×10^{12} (5.9×10^{12})	0.80 (0.38)
R6	$C_4H_3(CH_2O)O* + H* \leftrightarrow C_4H_3(CH_2OH)O* + *$	4.0×10^{12} (3.8×10^{12})	0.14 (0.83)	1.6×10^{13} (9.9×10^{12})	0.69 (0.83)	9.3×10^{12} (8.5×10^{12})	1.00 (0.88)
R7	$C_4H_3(CH_2OH)O* \rightarrow C_4H_3(CH_2OH)O(g) + *$	2.8×10^{16}	1.59	9.4×10^{15}	2.29	1.4×10^{14}	2.68
	Decarbonylation						
R8	$C_4H_3(CHO)O* + * \leftrightarrow C_4H_3(CO)O* + H*$	1.3×10^{14} (4.3×10^{12})	1.18 (1.09)	1.4×10^{14} (6.7×10^{12})	1.14 (1.12)	2.0×10^{13} (1.6×10^{12})	0.29 (0.79)
R9	$C_4H_3(CO)O* + * \leftrightarrow C_4H_3O* + CO*$	6.7×10^{12} (1.4×10^{12})	0.22 (0.75)	1.1×10^{14} (1.2×10^{13})	0.42 (1.31)	5.3×10^{13} (2.3×10^{11})	0.36 (1.17)
R10	$C_4H_3(CHO)O* + * \leftrightarrow C_4H_3O* + CHO*$	3.1×10^{13} (5.7×10^{10})	1.38 (1.28)	1.1×10^{14} (8.1×10^{11})	1.44 (1.45)	8.6×10^{13} (3.8×10^{10})	0.96 (1.15)
R11	$CHO* \leftrightarrow CO* + H*$	8.6×10^{12} (3.5×10^{12})	0.30 (0.98)	1.1×10^{13} (2.7×10^{12})	0.18 (1.13)	1.0×10^{13} (1.5×10^{13})	0.33 (1.55)
R12	$C_4H_3O* + H* \leftrightarrow C_4H_4O* + *$	1.4×10^{13} (2.8×10^{15})	0.84 (1.38)	7.3×10^{12} (1.9×10^{14})	0.71 (1.13)	5.2×10^{13} (2.0×10^{15})	0.72 (0.91)
R13	$C_4H_4O* \rightarrow C_4H_4O(g) + *$	3.1×10^{16}	1.31	3.9×10^{14}	2.09	1.7×10^{14}	2.41
R14	$CO* \rightarrow CO(g) + *$	2.9×10^{15}	0.98	9.9×10^{14}	1.13	1.2×10^{15}	1.80

An asterisk (*) represents a free site on the surface, species with an asterisk (*) indicates the adsorbed surface species.

metal atoms of the bottom two layers were fixed. To avoid unphysical interactions between the slabs, a vacuum slab of 18 and 16 Å was inserted between the surface slabs of Pt(111) and Pt(211), respectively. The Brillouin zone integration was performed using the Monkhorst-Pack scheme with (4×4×1) mesh for both surfaces. A nanocluster containing 55 Pt atoms (Pt_{55}) with a cubooctahedral shape was used to model the corner site of Pt nanoparticles. The free Pt_{55} nanocluster was immersed in the simulation box sizes of 25 Å × 25 Å × 25 Å. The single gamma points sampling schedule was used in the calculations of Pt_{55} nanoclusters.

The adsorption energy, E_{ad}, of the adsorbate such as reactant, intermediate and product on the model surface was calculated as

$$E_{ad} = E_{adsorbate+surface} - (E_{surface} + E_{adsorbate}) \quad (1)$$

where $E_{adsorbate+surface}$ is the total energy of the combined system of adsorbate on the metal surface slab or the cluster; $E_{surface}$ is the energy of the optimized clean surface slab or cluster; and $E_{adsorbate}$ is the energy of the adsorbate in vacuum. The energies include zero-point energy correlation. Based on this definition, a negative E_{ad} value indicates favorable (exothermic) adsorption.

All elementary reaction steps involved in the furfural reaction pathways were explored using the minimum-mode following dimer method.[36] Both the transition and the final states are located automatically. The dimer searching method is different from other transition state searching methods such as the climbing image-nudged elastic band (CI-NEB) method[37] in which both the initial and final states have to be determined before finding the transition state. The dimer searching method used in this work allows us to explore the unbiased reaction mechanism without prior knowledge of the possible final state (product) or chemical intuitions. In the present work, the dimer separation was set at 0.01 Å and the tolerance for force convergence to the transition state was less than 0.05 eV/Å. The identified transition state was further confirmed as being first-order saddle points using a finite-difference normal mode analysis. We also further confirmed several reaction pathways using the standard CI-NEB method. The reaction energy (ΔH) was calculated as the total energy difference between the final state and the initial state. The forward activation barrier (E_a) for each elementary step was defined as the total energy difference between the initial state and the transition state.

Microkinetic modeling

As we mentioned before, there are two competitive reaction routes, that is, hydrogenation and decarbonylation, in the furfural conversion in the presence of hydrogen over Pt catalysts. On the basis of previous experimental and theoretical work on various metal catalysts, only two important C—C bond scission steps are considered in this work.[9,10,12–15,24] A total of 14 elementary reaction steps involved in two reaction routes listed in Table 1 were used in the microkinetic modeling. In this work, the comprehensive microkinetic modeling was conducted by solving the differential equations describing the coverage of each surface intermediate.[38] All model parameters are rigorously derived from DFT calculations except for the sticking coefficients. The rate constants of surface reaction and desorption steps were calculated by $k_n = v\exp(-E_{a,n}/k_B T)$ using harmonic transition state theory. The pre-exponential factor (v) was the

ratio of positive normal mode frequencies of the initial state and saddle point ($v = \frac{\Pi_{i=1}^{N} v_i^{\text{initial}}}{\Pi_{j=1}^{N-1} v_j^{\dagger}}$).[39,40] The activation barrier ($E_{a,n}$) for the elementary reaction step (n) was calculated using dimer method. The rate constant of adsorption was calculated by $k_{ads}^{i} = S_0 P_i A_i / \sqrt{2\pi m_i k_B T}$. S_0 is the sticking coefficient of species i. Herein, the estimated values of 1×10^{-5} and 0.02 were used for furfural and H_2 on all three models, respectively. P_i and m_i are the partial pressure and mass of species i, respectively. A_i is the area of adsorption site.

Results and Discussion

Adsorption of reactants, intermediates, and products on Pt(111), Pt(211), Pt_{55}

Periodic DFT calculations were used to study the adsorption of furfural, reaction intermediates and products, as well as the reaction energetics of 14 elementary steps on the Pt(111), Pt(211) surfaces, and Pt_{55} nanocluster. Previous DFT calculations suggested that adsorption configuration of furfural plays a key role in the selectivity of furfural transformation on supported metal catalysts.[10,12–15] In the present work, various adsorption configurations of furfural over three Pt model catalyst surfaces are studied. The most favorable binding configurations of furfural, subsequent reaction intermediates, and products involved in the reaction mechanism at the terrace, step, and corner sites over the Pt(111), Pt(211) surfaces, and the Pt_{55} nanocluster are shown in Figure 2. We found the adsorption energies of all surface species on the three Pt model facets increase in the order of Pt(111) < Pt(211) < Pt_{55}, which agrees with the general adsorption trend that the adsorbate exhibits stronger adsorption strength at the low coordinated site on the metal surfaces.[41]

Furfural. On the flat Pt(111) surface, furfural adsorbs at the threefold hollow site with the carbonyl group tilting away from the surface. The optimized stable structure shows that the furanic ring of the adsorbed furfural is parallel to the surface plane, indicating that the binding energy (−1.36 eV) mainly comes from the interaction of unsaturated C═C bonds of the furanic ring with the Pt(111) surface. This is also consistent with reported furfural adsorption geometry by Liu et al.[42] On the stepped Pt(211) surface, furfural prefers to bind at the step site with an adsorption energy of −1.95 eV. As shown in Figure 2a, the furanic ring of the adsorbed furfural binds with two step surface Pt atoms with an averaged distance of 2.21 Å. The carbonyl group moves toward the Pt(211) surface and binds with another step Pt atom through O_2—Pt bond. The distances between the C_5 and O_2 of the carbonyl group and the step Pt atom are 2.48 and 2.19 Å, which are much shorter than the corresponding distances (2.92 and 3.16 Å) of the adsorbed furfural on Pt(111). On the Pt_{55} nanocluster, furfural adsorbs at the corner site with C_3 and C_4 atoms bonded with the same surface Pt atom and O_2 bonded to a surface Pt atom next to the corner site, leading to a tilted upright adsorption structure. The calculated adsorption energy of furfural on the Pt_{55} nanocluster is −2.52 eV.

Furfuryl Alcohol. The adsorption configurations of furfuryl alcohol on the three Pt model catalysts are shown in Figure 2b. The adsorption behavior of furfuryl alcohol is similar to furfural. The only exception is that the oxygenate ligand of furfuryl alcohol on the stepped Pt(211) surface tilts away from the surface after adding two H atoms on furfural. Our calculations show the adsorption energies of furfuryl alcohol are ~0.30 eV stronger than furfural on all three Pt model surfaces. A similar observation on Pt(111) was reported by Liu et al.[42]

Furan. The most stable adsorption configurations of furan on Pt model surfaces are shown in Figure 2c. The calculated adsorption energies of furan on Pt(111), Pt(211), and Pt_{55} are −1.31, −2.09, and −2.41 eV, respectively. Interestingly, we note that the adsorption strengths of furfural and furan on the three Pt catalyst models are similar. This suggests that that the carbonyl group of the adsorbed furfural has little interaction with the Pt surface.

Reaction Intermediates. The optimized adsorption structures of reaction intermediates in hydrogenation and decarbonylation reaction routes are illustrated in Figures 2d–g. For the hydrogenation intermediates of $C_4H_3(CHOH)O$ and $C_4H_3(CH_2O)O$, the adsorption behaviors are very similar to furfural, except that the oxygenate ligands of $C_4H_3(CHOH)O$ are slightly pushed away from the surface after the first hydrogenation of furfural at O_2 position. The calculated adsorption energies of $C_4H_3(CH_2O)O$ on the Pt(111), Pt(211), and Pt_{55} are −3.12, −3.99, and −4.50 eV, respectively, which are much higher than the adsorption energies of −2.29, −2.88, and −3.40 eV for $C_4H_3(CHOH)O$. This suggests that the stronger interaction between the CH_2O group and Pt surface than the interaction between the CHOH group and Pt surface. After the dehydrogenation reaction, the O_2 atom in $C_4H_3(CO)O$ tilts away from the surface, while C_5 atom turns to bind at the atop site with the C_5—Pt distances of 1.96, 2.01, and 1.98 Å on Pt(111), Pt(211), and Pt_{55}, respectively. The stronger interaction between the carbonyl group and the surface also makes the furanic ring tilts away from the surface. For the decarbonylation intermediate of C_4H_3O, it adsorbs strongly in upright configuration with the adsorption energies of −3.74, −4.46, and −5.10 eV on the Pt(111), Pt(211), and Pt_{55}.

Reaction pathways for furfural hydrogenation and decarbonylation

Furfural hydrogenation and decarbonylation are two major reaction routes for furfural transformation in the presence of hydrogen over metal catalysts (Figure 1). To gain fundamental insights into the structural effect on the selectivity of furfural conversion, we calculated all the elementary reaction steps involved in both hydrogenation and decarbonylation on the three Pt catalyst model surfaces. For each model surface, we start with the most stable furfural configuration at the specific site on each surface. The calculated activation barriers and reaction energies of elementary reaction steps are summarized in Table 1. The transition state structures of elementary steps on three Pt model catalyst surfaces are shown in Figure 3.

Furfural Hydrogenation. In the hydrogenation route, furfural undergoes two consecutive hydrogenation steps to form furfuryl alcohol. Depending on the first hydrogenation step occurs at which position (C_5 or O_2), two hydrogenation scenarios are possible. In the first scenario, the first hydrogen atom is added onto the O_2 position, followed by the addition of second hydrogen atom at the C_5 position. While the second hydrogenation scenario is just vice versa. The calculated potential energy profiles of the two furfural hydrogenation scenarios on the three Pt catalyst models are shown in Figure 4. First, we note that the overall hydrogenation of furfural into furfuryl alcohol on Pt(111) is exothermic while it is nearly neutral on the Pt(211) and endothermic on Pt_{55} cluster. This suggests that the flat Pt(111) surfaces are thermodynamically

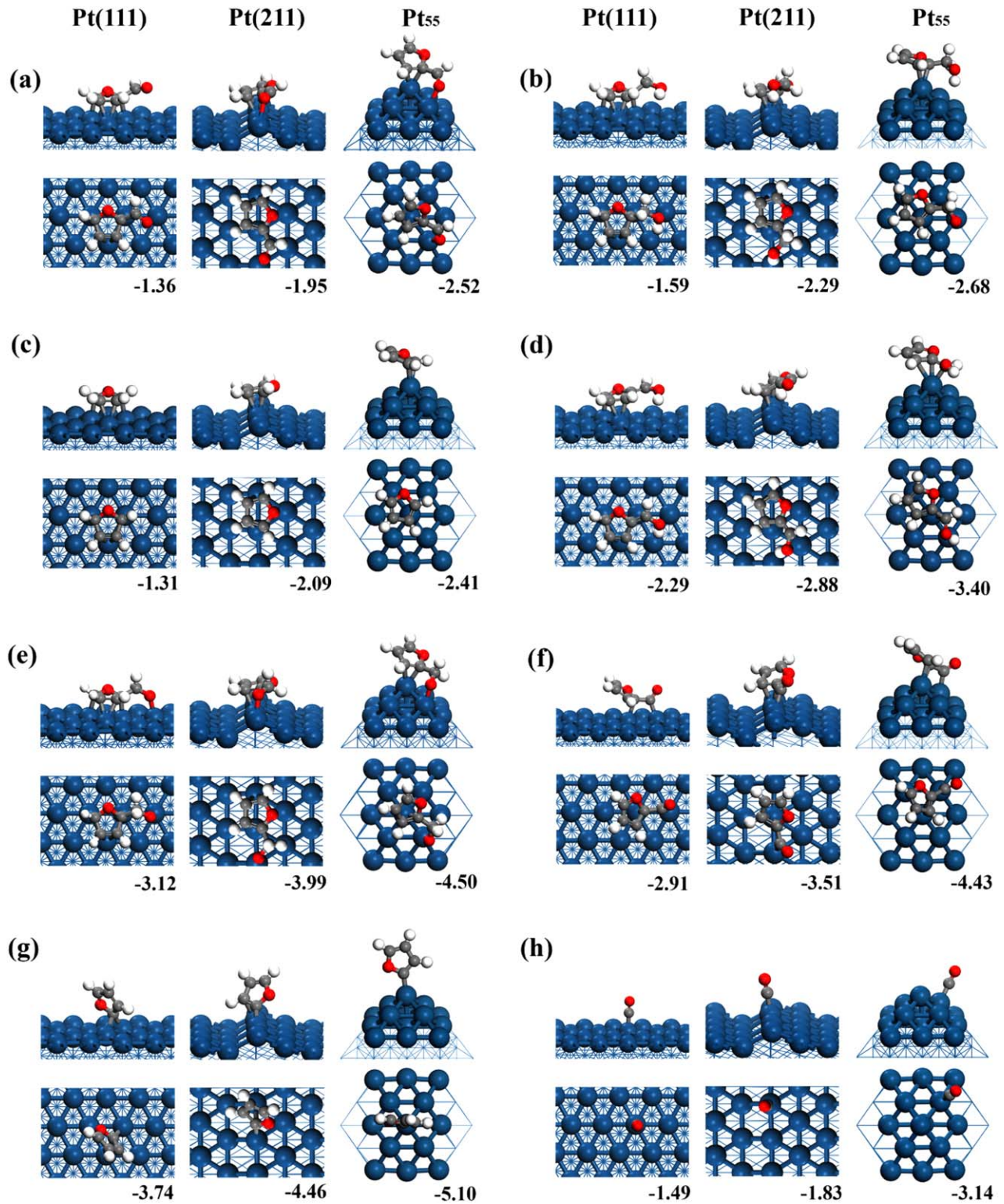

Figure 2. Optimized adsorption configurations of (a) $C_4H_3(CHO)O$; (b) $C_4H_3(CH_2OH)O$; (c) C_4H_4O; (d) $C_4H_3(CHOH)O$; (e) $C_4H_3(CH_2O)O$; (f) $C_4H_3(CO)O$; (g) C_4H_3O; and (h) CO on Pt(111), Pt(211), and Pt_{55}.

The side and top views of optimized structures are shown in upper and lower panels, respectively. Pt, C, O, and H atoms are in blue, gray, red, and white colors, respectively. [Color figure can be viewed in the online issue, which is available at wileyonlinelibrary.com.]

more favorable for furfural hydrogenation than the stepped Pt(211) surface and the Pt_{55} nanocluster. Second, on the Pt(111) surface, the calculated activation barriers of the first and second hydrogenation steps in first scenario are both 0.34 eV. While the barriers of the first and the second hydrogenation steps in the second hydrogenation scenario are 0.71 and 0.14 eV. This indicates that the first hydrogenation scenario on the Pt(111) surface is kinetically more favorable than the second hydrogenation scenario. The same preference was also identified on the Pd(111) using DFT calculations.[24] We also

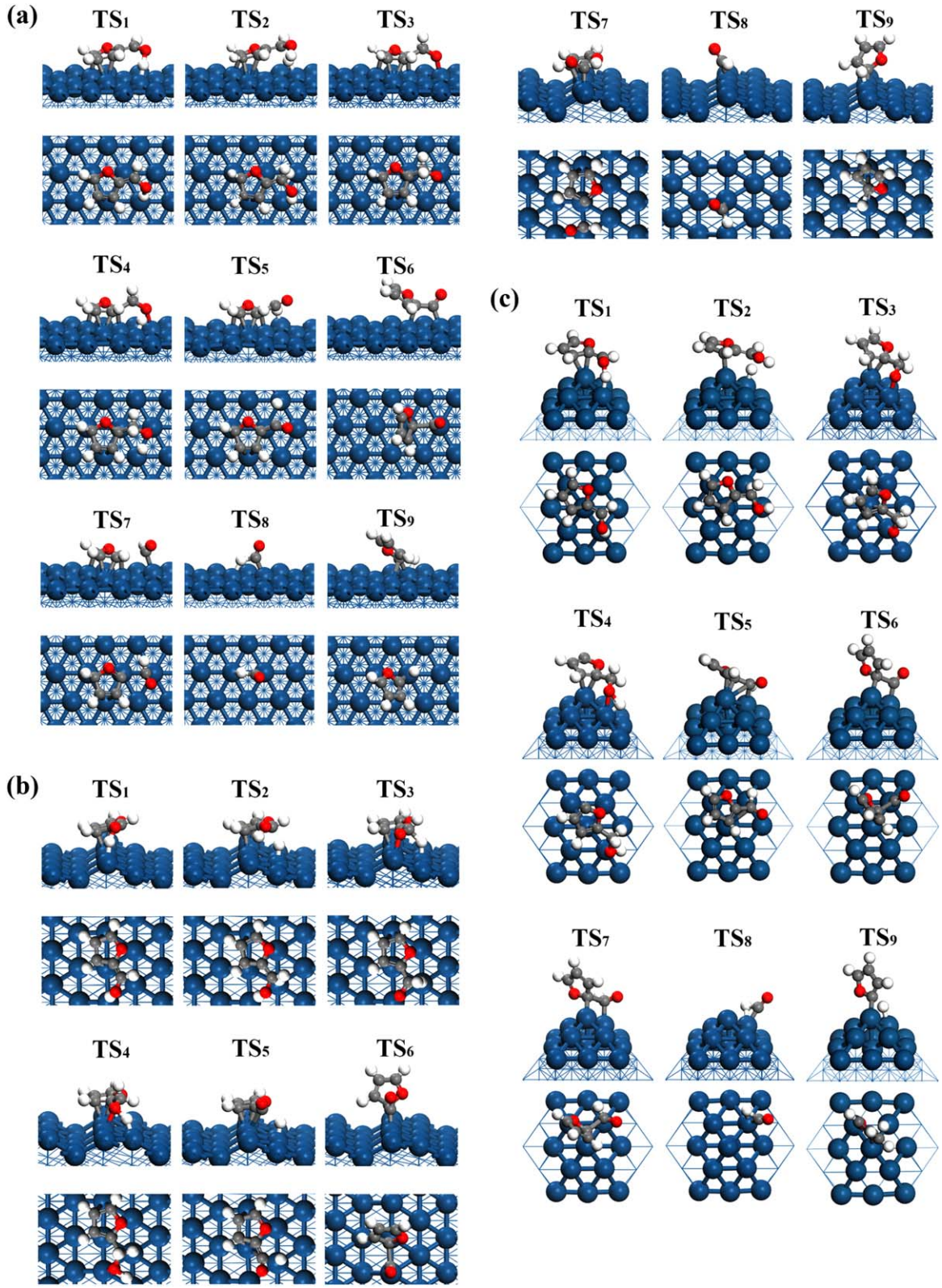

Figure 3. Transition state structures of furfural hydrogenation and decarbonylation reactions on (a) Pt(111); (b) Pt(211); (c) Pt_{55}.

The number listed below the figure is the adsorption energy in eV. [Color figure can be viewed in the online issue, which is available at wileyonlinelibrary.com.]

note that Liu et al. studied two furfural hydrogenation scenarios on Pt(111) using different GGA functionals (PW91 and optB86b).[42] They found that the activation barriers for the first and second hydrogenation steps in the first hydrogenation scenario are 0.48 and 1.12 eV using PW91 functional while they are 0.41 and 0.79 eV using optB86b functional. For the second hydrogenation scenario, the barriers for two sequential hydrogenation steps are 0.52 and 0.61 eV using PW91 and 0.38 and

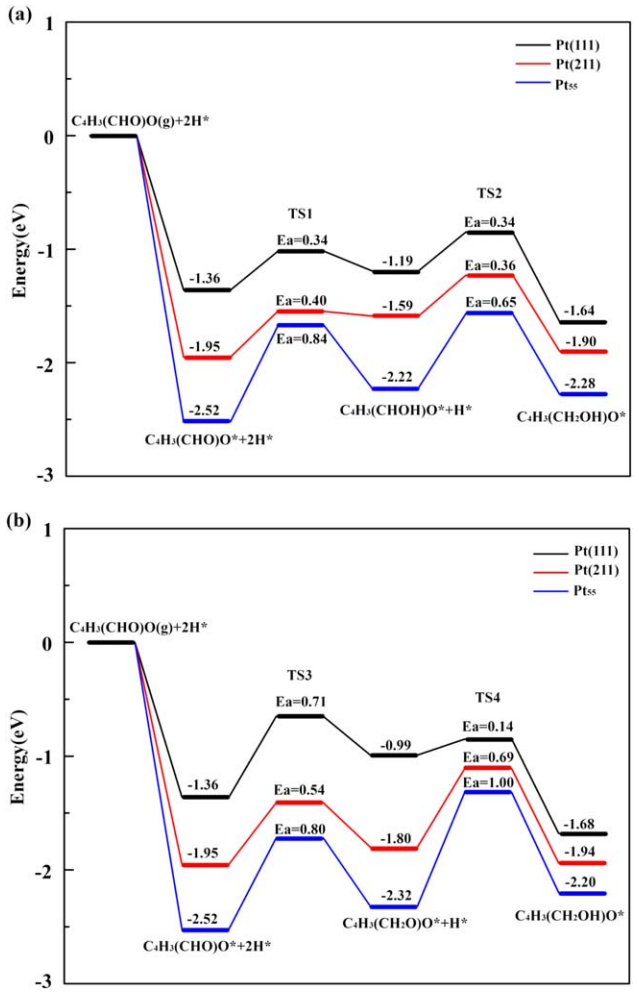

Figure 4. Potential energy profiles of furfural hydrogenation in the (a) first and (b) second scenario on Pt(111), Pt(211), and Pt_{55}.

[Color figure can be viewed in the online issue, which is available at wileyonlinelibrary.com.]

0.60 eV using optB86b. Although the choice of different functionals and vdW interactions results in difference reaction barrier, their calculations suggested that the two hydrogenation scenarios are kinetically competitive on Pt(111). This is in general consistent with our calculation results in the present work.

Our calculation results show that two hydrogenation scenarios becomes competitive when the surface structure shifts from the flat Pt(111) surface to the stepped Pt(211) surface and the Pt_{55} cluster. The activation barrier for the first hydrogenation step in the first and second hydrogenation scenarios are 0.40 and 0. 54 eV on Pt(211) surface, while they are 0.84 and 0.80 eV on Pt_{55} cluster. As a result, the first hydrogenation step in both scenarios are kinetically competitive on Pt(211) and Pt_{55}. While the barrier of second hydrogenation step in the first scenario is about 0.3 eV lower than that in the second scenario on both Pt(211) and Pt_{55}, making the first scenario kinetically a little more favorable than the second scenario.

Furfural Decarbonylation. Similar to the furfural hydrogenation, two different scenarios in the furfural decarbonylation were also considered. In the first decarbonylation scenario, the furfural undergoes dehydrogenation step via the C_5—H bond scission, followed by the decarbonylation step via the C_4—C_5 bond breaking. In the second decarbonylation scenario, the C_4—C_5 bond of the furfural is first broken forming the furanic (C_4H_3O) intermediate and the carbonyl group (CHO). The carbonyl group then further decomposes into the atomic H and CO. The final step in furfural decarbonylation is that the formed C_4H_3O is hydrogenated at the C_4 positon forming furan as the major product. The calculated potential energy profiles of furfural decarbonylation on three Pt model surfaces are shown in Figure 5. Different from the furfural hydrogenation, the low-coordinated sites on the Pt(211) surface and the Pt_{55} cluster are thermodynamically more favorable than the flat Pt(111) surface for furfural decarbonylation.

Our calculation results show that the barriers of first steps (dehydrogenation) in the first scenario are 1.18 and 1.14 eV on Pt(111) and Pt(211), which are a little lower than that of the first step (decarbonylation) in the second scenario by 0.20 and 0.30 eV. While the barriers in the second steps are much lower than the corresponding previous steps in both the two scenarios. These imply that the first scenario is kinetically a little morefavorable on both Pt(111) and Pt(211). The barriers of the first and the second steps in first decarbonylation scenario on Pt_{55} are 0.29 and 0.36 eV, while the barriers of the first and the second steps in the second decarbonylation scenario are

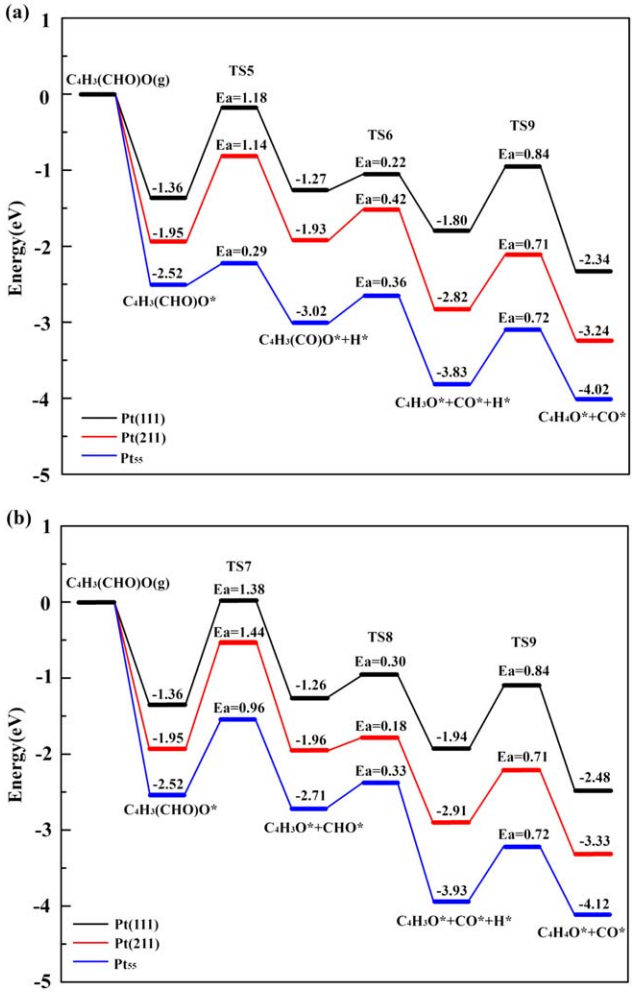

Figure 5. Potential energy profiles of furfural decarbonylation in the (a) first and (b) second scenario on Pt(111), Pt(211), and Pt_{55}.

[Color figure can be viewed in the online issue, which is available at wileyonlinelibrary.com.]

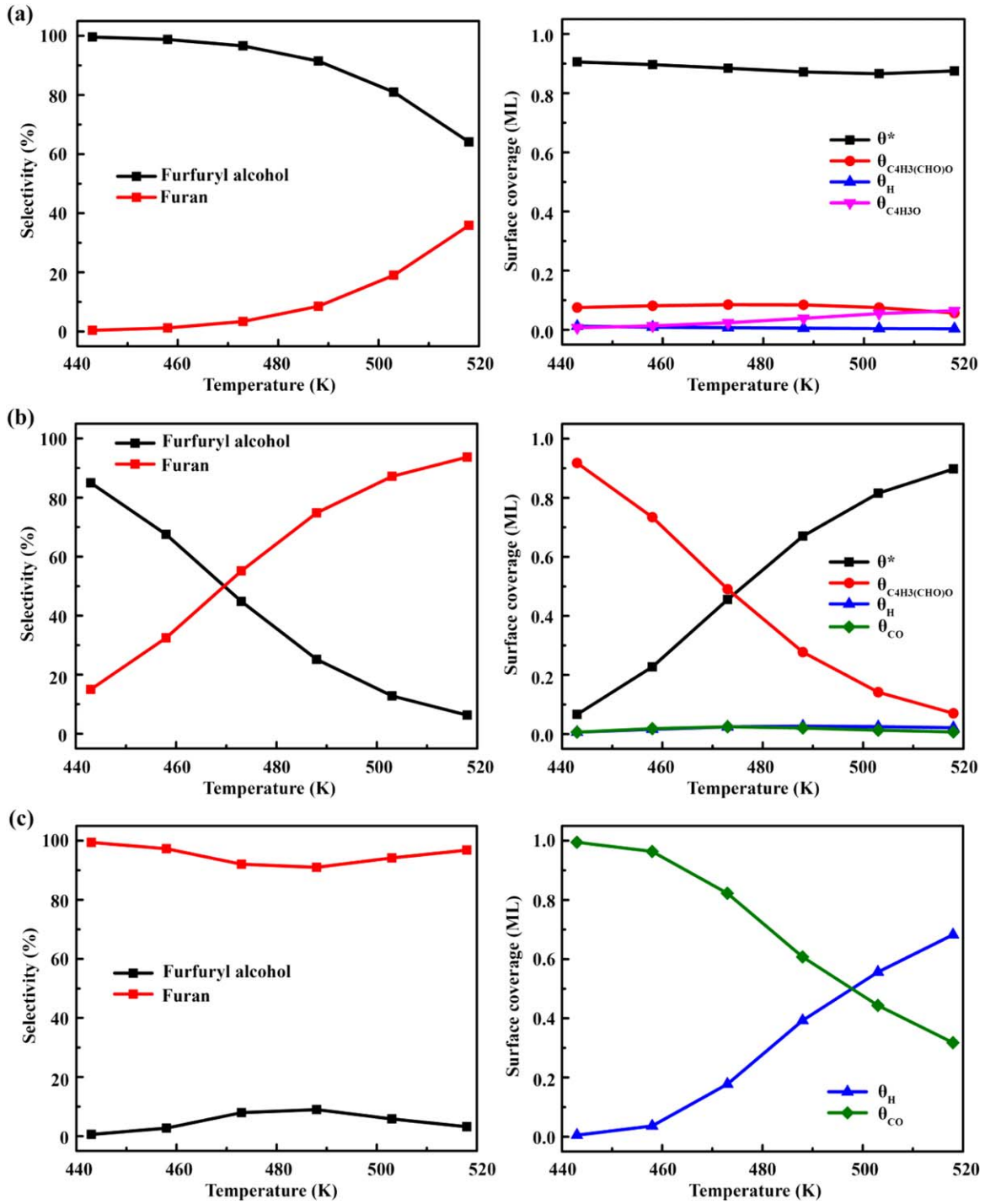

Figure 6. The product selectivity (left) and steady-state surface coverage (right) as a function of temperature ($P_{C_4H_3(CHO)O}$ = 9.3 kPa and P_{H_2} = 93 kPa) on (a) Pt(111); (b) Pt(211); (c) Pt_{55}.

The species with surface coverage less than 0.01 are not shown in the figure. [Color figure can be viewed in the online issue, which is available at wileyonlinelibrary.com.]

0.96 and 0.33 eV. It is expected that the first decarbonylation scenario is kinetically much more favorable on Pt_{55}.

As aforementioned, the selectivity of furfural conversion in the presence of hydrogen over Pt catalysts is determined by the dominant reaction pathway under reaction conditions. Comparing the calculated reaction energies and activation barriers for furfural hydrogenation and decarbonylation pathways shown in Figures 4 and 5, it is clear that the furfural hydrogenation pathway will be kinetically favorable on the Pt(111) and the Pt(211) surfaces even though the furfural decarbonylation pathway is thermodynamically more feasible. On the Pt_{55} nanocluster, the furfural decarbonylation pathway is both thermodynamically and kinetically more favorable. As such, our DFT results suggest that the furan is the major product via furfural decarbonylation over smaller Pt nanoparticle catalysts with more corner sites while the furfuryl alcohol is the major product via furfural hydrogenation over larger Pt catalysts with more flat and stepped surface structures exposed.

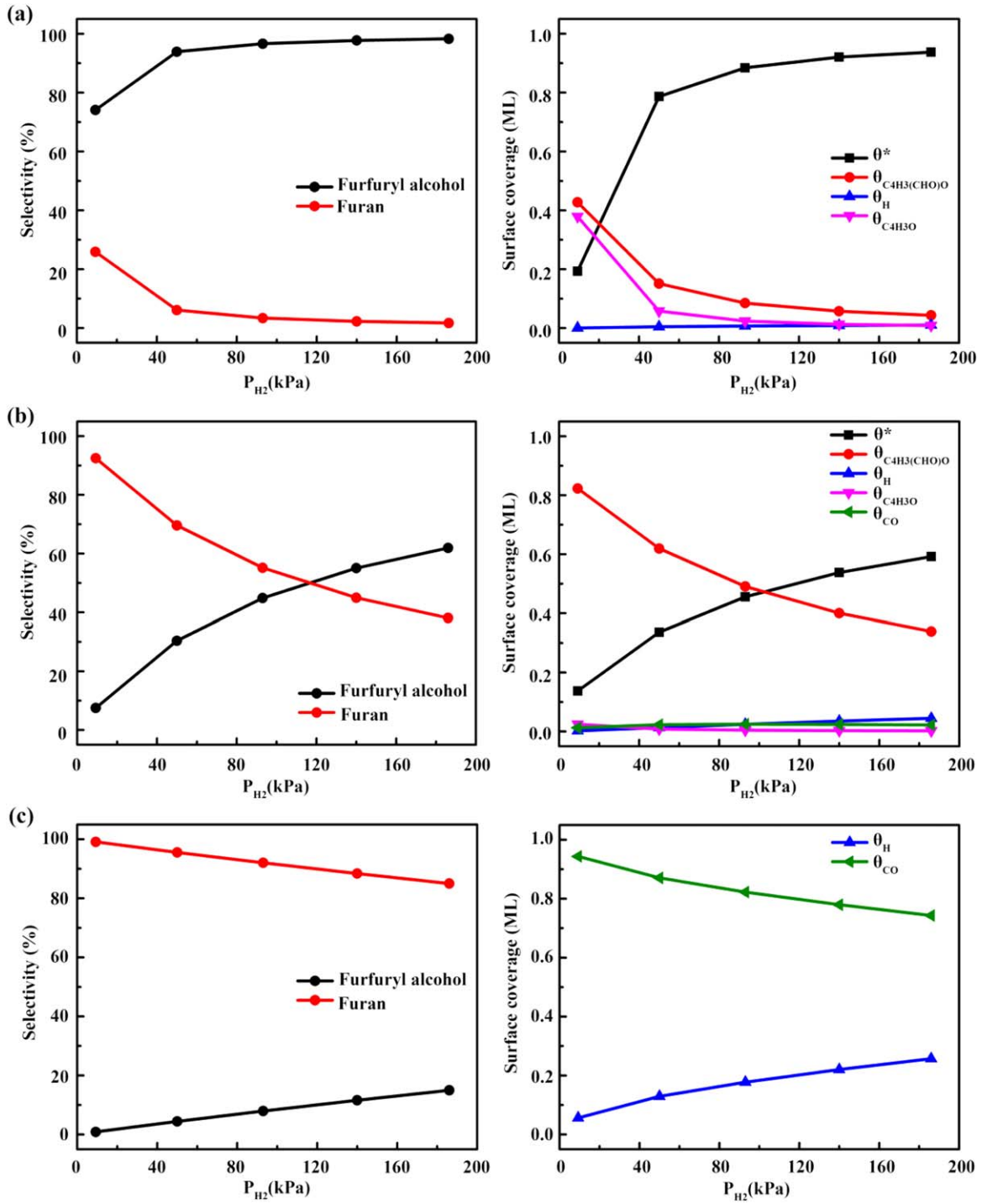

Figure 7. The product selectivity (left) and steady-state surface coverage (right) as a function of hydrogen partial pressure ($P_{C_4H_3(CHO)O}$ = 9.3 kPa and T = 473 K) on (a) Pt(111); (b) Pt(211); (c) Pt_{55}.

The species with surface coverage less than 0.01 are not shown in the figure. [Color figure can be viewed in the online issue, which is available at wileyonlinelibrary.com.]

Microkineitc modeling

To further confirm the above mechanistic insight into the surface structure effects on the furfural selectivity on the basis of our DFT calculation results, and most importantly, to correlate our DFT results with the experimentally measured selectivity as a function of the Pt catalyst particle size and reaction condition, a microkinetic model including 14 elementary reaction steps was developed in this work. In the microkinetic model, the kinetics database from our DFT results shown in Table 1 are used as input parameters for the rate constant calculation. Considering experimental measurements were performed in a tubular plug flow reactor, the activation barriers for CO desorption are adjusted to 0.98 (1.48) eV on Pt(111), 1.13 (1.83) eV on Pt(211), and 1.80 (3.14) eV on Pt_{55} to avoid the unrealistic CO poisoning with DFT calculated CO binding energies in parenthesis. It is assumed that the products (furfuryl alcohol and furan) will directly desorb from the catalyst surface once produced. The criteria for these adjustments is to

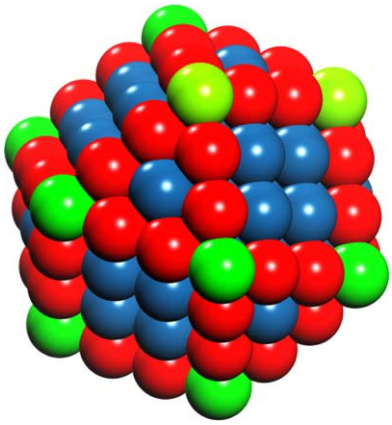

Figure 8. The cubooctahedral nanoparticle model.

The terrace, step, and corner atom sites are shown in blue, red, and green, respectively. [Color figure can be viewed in the online issue, which is available at wileyonlinelibrary.com.]

make sure the intrinsic reaction kinetics is not controlled by either the adsorption of reactant or the desorption of the products. The steady-state surface coverages are calculated by solving the differential equations describing the coverage of each surface intermediate. The individual elementary reaction rates are calculated using the steady-state surface coverages (θ, monolayer [ML]). The effects of lateral interactions at high surface coverage on reaction rates are not considered in the modeling. The selectivity for furfuryl alcohol is calculated by $S = (r_4 + r_6)/(r_4 + r_6 + r_{12})$, where r_4 and r_6 are the furfuryl alcohol formation rates via the first and second scenarios, respectively; r_{12} is the furan formation rate. All rates are in the unit of s^{-1}.

Figure 6 shows the temperature effect on the product selectivity and surface coverages on three Pt model catalyst surfaces at partial pressures of $P_{C_4H_3(CHO)O} = 9.3$ kPa and $P_{H_2} = 93$ kPa. On the Pt(111) surface, the selectivity of furfuryl alcohol decreases from 99.6% at 443 K to 64.1% at 518 K. This indicates that the hydrogenation is the dominant route on Pt(111), especially at low temperatures. We note the total surface coverage is very low under studied condition. The surface is only covered by furfural (0.07–0.09 ML) and trace amounts of hydrogen and the decarbonylation intermediate C_4H_3O. This suggests that all the hydrogenation steps in the hydrogenation route are fast on the Pt(111) surface while the hydrogenation of C_4H_3O is the rate-limiting step in the minor decarbonylation reaction route. As the temperature increases, the rates of both decarbonylation step (R_9 and R_{10}) and C_4H_3O hydrogenation step (R_{12}) increase. As a result, the surface coverage of C_4H_3O increases from 0.007 to 0.055 ML while the hydrogen surface coverage decreases from 0.012 to 0.004 ML. On the Pt(211) surface, the selectivity of furfuryl alcohol decreases from 85.0% at 443 K to 6.3% at 518 K. At 470 K, the furfural selectivity shifts from furfuryl alcohol to furan. Unlike the Pt(111) surface, the furfural coverage on the Pt(211) surface is high in the low temperature range. With increasing temperature, the furfural coverage decreases from 0.919 ML at 443 K to 0.062 ML at 518 K. For the Pt_{55} nanocluster, the decarbonylation reaction route is dominant in the furfural conversion with the selectivity to furan higher than 92% in the studied temperature range. Our modeling results show that CO becomes the dominant surface species on the Pt_{55} nanocluster. At 443 K, all the corner sites on the Pt_{55} nanocluster surface are fully covered by CO, indicating the possible deactivation of the Pt catalyst by CO poison. At this condition, the activity of decarbonylation is largely dependent upon the availability of empty sites for furfural adsorption. With increasing temperature, the CO coverage drops due to the increasing CO desorption rate. As a result, the hydrogen adsorption becomes more competitive. However, the furfural adsorption is still limited by the availability of empty sites. Our microkinetic modeling results clearly indicate that the formation of furfuryl alcohol is favored at low temperatures but the formation of furan becomes significant at high temperatures on both Pt(111) and Pt(211) surfaces. For the Pt_{55} nanocluster, the selectivity of furan is always more than 90% at all temperature range.

We also investigate the effect of hydrogen partial pressure (9.3–186 kPa) on the furfural selectivity at 473 K. As shown in Figure 7, the selectivity to furfuryl alcohol monotonically increases with increasing hydrogen partial pressure on three model surfaces. On the Pt(111) and Pt(211) surfaces, the furfural surface coverage decreases while the empty site increases as the hydrogen partial pressure increasing. Surprisingly, the hydrogen partial pressure has no effect on the hydrogen coverage. Hydrogen surface coverage is very low (<0.01 ML) on both Pt(111) and Pt(211) surfaces, suggesting the hydrogenation reaction rate is affected by the limited hydrogen coverage although the hydrogen partial pressure is increased. It is also noted that the large difference of C_4H_3O surface coverages between Pt(111) and Pt(211) surfaces especially at low hydrogen partial pressure condition. At $P_{H_2} = 9.3$ kPa, the C_4H_3O surface coverage is 0.38 ML on Pt(111) while it is very low (0.03 ML) on Pt(211). This is ascribed to the fact that the fast hydrogenation steps in the hydrogenation route consumed the limited hydrogen atoms that might participate in the hydrogenation of C_4H_3O in the decarbonylation route on Pt(111).

We note that the assumptions such as the low sticking coefficients, direct desorption of product, weakened CO binding energy in the microkinetic model lead to lower coverage of intermediates on the surface. However, these assumptions did not change the trend of the selectivity. We have tested our model at high coverages of reactants, intermediates, and products using unadjusted DFT binding energies that were calculated in this work. As shown in Supporting Information Figure S2, we found that the terrace surface was mostly covered by CO. The total coverage of all surface intermediates is ~0.8 ML. At this high coverage condition, the predicted selectivities of products are nearly the same as the results at low coverage condition.

Previous studies have suggested that the fractions of exposed surface structures or site types (e.g., terrace, step, and corner) are a function of the catalyst particle size.[41,43] In the present study, the flat Pt(111) surface, stepped Pt(211) surface,

Table 2. Estimated Fractions of Three Typical Surface Structures (Terrace, Step, and Corner) as a Function of the Cubooctahedral Pt Nanoparticle Size

Particle Size (nm)	Terrace	Step	Corner
0.6	0	0	100
1.1	14.29	57.14	28.57
1.7	34.78	52.18	13.04
2.8	57.14	38.09	4.77
3.4	63.54	33.15	3.31
4.4	71.96	26.17	1.87
5.5	77.24	21.56	1.20

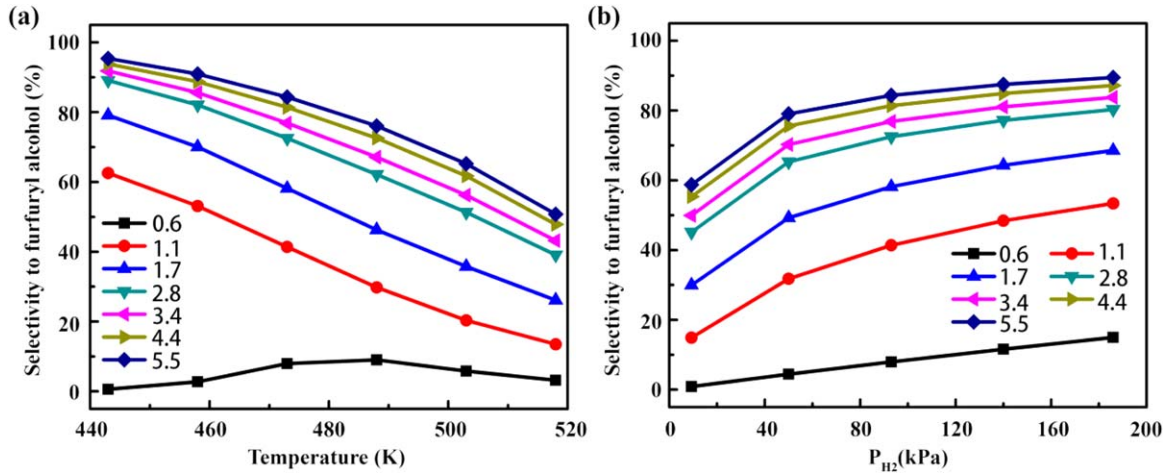

Figure 9. The predicted selectivity as a function of the Pt nanoparticle size (in nm).

(a) In the temperature range of 443–518 K ($P_{C_4H_3(CHO)O}$ = 9.3 kPa and P_{H_2} = 93 kPa); (b) in the hydrogen partial pressure range of 9.3–186 kPa at 473 K. [Color figure can be viewed in the online issue, which is available at wileyonlinelibrary.com.]

and Pt_{55} nanocluster are used to represent the terrace, step, and corner sites. We assume the supported Pt catalysts used in the experiments are all in the same cubooctahedral shape of various sizes (Figure 8). With this assumption, the fractions of three typical surface structure sites as a function of the particle size can be calculated. Table 2 lists the fractions of three surface sites ranging from 0.6 to 5.5 nm. Therefore, the total product (furfuryl alcohol or furan) selectivity over a certain size of Pt catalyst can be estimated[44]

$$S = S_{\text{terrace}} \times f_{\text{terrace}} + S_{\text{step}} \times f_{\text{step}} + S_{\text{corner}} \times f_{\text{corner}} \quad (2)$$

where S_i and f_i are the product selectivity and the fraction of the type of surface site i, respectively. Herein, we have to mention that the spatial hindrance induced by the strong adsorption of stepped and corner sites or different adsorption configurations, as well as lateral interactions between surface reaction species under high coverages are not rigorously described.

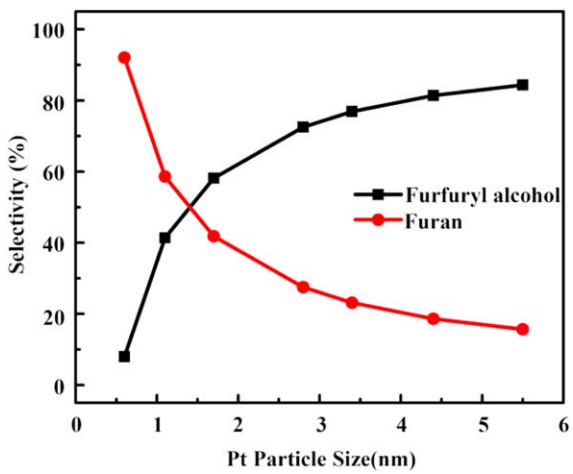

Figure 10. The predicted selectivity as a function of the Pt nanoparticle size at T = 473 K and P_{H_2} = 93 kPa ($P_{C_4H_3(CHO)O}$ = 9.3 kPa).

[Color figure can be viewed in the online issue, which is available at wileyonlinelibrary.com.]

The steady-state product selectivity of furfural transformation in the temperature range of 443–518 K as a function of Pt nanoparticle size is investigated. For the Pt nanoparticle size larger than 1.1 nm, the selectivity of furfuryl alcohol decreases with increasing temperature while the furfuryl alcohol selectivity is only slightly affected on the smallest particle size of 0.6 nm. This is consistent with the reported selectivity trend in the previous experiment.[11] As shown in Figure 9a, our modeling results show that the furfuryl alcohol selectivity over the Pt particle of 0.6 nm are 0.6–9.0% in the temperature range of 443–518 K, which is in agreement with experimentally measured values of ~5% for the Pt catalyst of 1.5 nm.[11] Similarly, for the larger Pt particle of 5.5 nm, the modeling prediction of the furfuryl alcohol selectivity decreases from 95.8 to 50.2% as the temperature increases from 443 to 518 K, this is also consistent with the measured 80 to 50% over the Pt particle size of 5.9 nm.[11] We also investigate the steady-state product selectivity of furfural transformation in the hydrogen partial pressure range of 9.3–186 kPa as a function of Pt nanoparticle size. As the hydrogen partial pressure increases, the selectivity of furfuryl alcohol increases independent of the Pt nanoparticles size (Figure 9b).

Figure 10 shows the predicted furfural selectivity at T = 473 K and P_{H_2} = 93 kPa as a function of the Pt nanoparticle size. The reaction selectivity in the furfural conversion shifts from furan to furfuryl alcohol at the particle size of 1.4 nm, which is only slightly smaller than the reported experimental value of 2.5 nm at the same condition.[11] It is concluded that the selectivity prediction from our microkinetic modeling shows similar product selectivity trend that the decarbonylation route dominants over smaller Pt nanoparticles while the hydrogenation route becomes significant on larger Pt nanoparticles at T = 473 K and P_{H_2} = 93 kPa.

Conclusions

In present work, the origin of the particle size-dependent selectivity for furfural conversion over Pt catalysts has been studied using the combination of DFT calculations and microkinetic modeling. Three Pt model surface structures, that is,

the flat Pt(111), stepped Pt(211), and Pt_{55} cluster are chosen to represent the terrace, step, and corner sites of the Pt nanoparticle. DFT calculations of furfural conversion in the presence of hydrogen over three Pt model structure surfaces show that the activation barriers for the furan formation are much higher than those for the formation of furfuryl alcohol at the terrace and the step sites while the opposite trend is found at the corner site. On the basis of DFT results, a microkinetic modeling is developed to investigate the effects of temperature, hydrogen pressure, and particle size on the furfural transformation selectivity. It is found that the production of furfuryl alcohol on the terrace and step sites is favored at low temperatures. Conversely, the formation of furan is preferred on corner sites. Under experimental operating condition of $T = 473$ K and $P_{H_2} = 93$ kPa, the decarbonylation route dominants on the Pt particle below 1.4 nm in size while the furfural hydrogenation prevails on the Pt particles larger than 1.4 nm. Our modeling results are in good agreement with previous experimental observation. Therefore, the methodology developed in the present study can be also applicable to numerous other size-dependent activity/selectivity reactions.

Acknowledgments

This work was supported by National Basic Research Program of China (973 Program) (2013CB733501) and the National Natural Science Foundation of China (NSFC-21306169, 21176221, 21136001, 21101137, and 91334103). This work was also partially supported by the US Department of Energy (DOE), the Office of Basic Energy Sciences, Division of Chemical Sciences, Geosciences & Biosciences. Pacific Northwest National Laboratory (PNNL) is a multi-program national laboratory operated for DOE by Battelle. Computing time was granted by the grand challenge of computational catalysis of the William R. Wiley Environmental Molecular Sciences Laboratory (EMSL). EMSL is a national scientific user facility located at Pacific Northwest National Laboratory (PNNL) and sponsored by DOE's Office of Biological and Environmental Research.

Literature Cited

1. Dutta S, De S, Saha B, Alam MI. Advances in conversion of hemicellulosic biomass to furfural and upgrading to biofuels. *Catal Sci Technol*. 2012;2(10):2025–2036.
2. Elliott DC, Hart TR. Catalytic hydroprocessing of chemical models for bio-oil. *Energy Fuel*. 2009;23(1):631–637.
3. Huber GW, Iborra S, Corma A. Synthesis of transportation fuels from biomass: chemistry, catalysts, and engineering. *Chem Rev*. 2006;106(9):4044–4098.
4. Czernik S, Bridgwater AV. Overview of applications of biomass fast pyrolysis oil. *Energy Fuels*. 2004;18(2):590–598.
5. Saidi M, Samimi F, Karimipourfard D, Nimmanwudipong T, Gates BC, Rahimpour MR. Upgrading of lignin-derived bio-oils by catalytic hydrodeoxygenation. *Energy Environ Sci*. 2014;7(1):103–129.
6. Serrano-Ruiz JC, West RM, Durnesic JA. Catalytic conversion of renewable biomass resources to fuels and chemicals. *Annu Rev Chem Biomol Eng*. 2010;1:79–100.
7. Nakagawa Y, Tamura M, Tomishige K. Catalytic reduction of biomass-derived furanic compounds with hydrogen. *ACS Catal*. 2013;3(12):2655–2668.
8. Wang H, Male J, Wang Y. Recent advances in hydrotreating of pyrolysis bio-oil and its oxygen-containing model compounds. *ACS Catal*. 2013;3(5):1047–1070.
9. Pang SH, Medlin JW. Adsorption and reaction of furfural and furfuryl alcohol on Pd(111): unique reaction pathways for multifunctional reagents. *ACS Catal*. 2011;1(10):1272–1283.
10. Pang SH, Schoenbaum CA, Schwartz DK, Medlin JW. Directing reaction pathways by catalyst active-site selection using self-assembled monolayers. *Nat Commun*. 2013;4:2448.
11. Pushkarev VV, Musselwhite N, An K, Alayoglu S, Somorjai GA. High structure sensitivity of vapor-phase furfural decarbonylation/hydrogenation reaction network as a function of size and shape of Pt nanoparticles. *Nano Lett*. 2012;12(10):5196–5201.
12. Sitthisa S, An W, Resasco DE. Selective conversion of furfural to methylfuran over silica-supported Ni-Fe bimetallic catalysts. *J Catal*. 2011;284(1):90–101.
13. Sitthisa S, Resasco DE. Hydrodeoxygenation of furfural over supported metal catalysts: a comparative study of Cu, Pd and Ni. *Catal Lett*. 2011;141(6):784–791.
14. Sitthisa S, Sooknoi T, Ma Y, Balbuena PB, Resasco DE. Kinetics and mechanism of hydrogenation of furfural on Cu/SiO_2 catalysts. *J Catal*. 2011;277(1):1–13.
15. Sitthisa S, Trung P, Prasomsri T, Sooknoi T, Mallinson RG, Resasco DE. Conversion of furfural and 2-methylpentanal on Pd/SiO_2 and $Pd\text{-}Cu/SiO_2$ catalysts. *J Catal*. 2011;280(1):17–27.
16. Zhang W, Zhu Y, Niu S, Li Y. A study of furfural decarbonylation on K-doped Pd/Al_2O_3 catalysts. *J Mol Catal A Chem*. 2011;335(1–2):71–81.
17. Zhao Y. Facile synthesis of Pd nanoparticles on SiO_2 for hydrogenation of biomass-derived furfural. *Environ Chem Lett*. 2014;12(1):185–190.
18. Yan K, Chen A. Selective hydrogenation of furfural and levulinic acid to biofuels on the ecofriendly Cu-Fe catalyst. *Fuel*. 2014;115:101–108.
19. Yan K, Wu G, Lafleur T, Jarvis C. Production, properties and catalytic hydrogenation of furfural to fuel additives and value-added chemicals. *Renew Sustain Energy Rev*. 2014;38:663–676.
20. Yan K, Jarvis C, Lafleur T, Qiao Y, Xie X. Novel synthesis of Pd nanoparticles for hydrogenation of biomass-derived platform chemicals showing enhanced catalytic performance. *RSC Adv*. 2013;3(48):25865–25871.
21. Lange J-P, van der Heide E, van Buijtenen J, Price R. FurfuralaA promising platform for lignocellulosic biofuels. *ChemSusChem*. 2012;5(1):150–166.
22. Norskov JK, Bligaard T, Rossmeisl J, Christensen CH. Towards the computational design of solid catalysts. *Nat Chem*. 2009;1(1):37–46.
23. van Santen RA, Ghouri MM, Shetty S, Hensen EMH. Structure sensitivity of the Fischer-Tropsch reaction; molecular kinetics simulations. *Catal Sci Technol*. 2011;1(6):891–911.
24. Vorotnikov V, Mpourmpakis G, Vlachos DG. DFT study of furfural conversion to furan, furfuryl alcohol, and 2-methylfuran on Pd(111). *ACS Catal*. 2012;2(12):2496–2504.
25. Somorjai GA, Materer N. Surface structures in ammonia synthesis. *Top Catal*. 1994;1(3–4):215–231.
26. Rioux RM, Hsu BB, Grass ME, Song H, Somorjai GA. Influence of particle size on reaction selectivity in cyclohexene hydrogenation and dehydrogenation over silica-supported monodisperse Pt particles. *Catal Lett*. 2008;126(1–2):10–19.
27. Kuhn JN, Huang W, Tsung C-K, Zhang Y, Somorjai GA. Structure sensitivity of carbon-nitrogen ring opening: impact of platinum particle size from below 1 to 5 nm upon pyrrole hydrogenation product selectivity over monodisperse platinum nanoparticles loaded onto mesoporous silica. *J Am Chem Soc*. 2008;130(43):14026.
28. Kresse G, Furthmuller J. Efficient iterative schemes for ab initio total-energy calculations using a plane-wave basis set. *Phys Rev B*. 1996;54(16):11169–11186.
29. Kresse G, Furthmuller J. Efficiency of ab-initio total energy calculations for metals and semiconductors using a plane-wave basis set. *Comput Mater Sci*. 1996;6(1):15–50.
30. Kresse G, Hafner J. Ab-initio molecular-dynamics simulation of the liquid-metal amorphous-semiconductor transition in germanium. *Phys Rev B*. 1994;49(20):14251–14269.
31. Blochl PE. Projector augmented-wave method. *Phys Rev B*. 1994;50(24):17953–17979.
32. Kresse G, Joubert D. From ultrasoft pseudopotentials to the projector augmented-wave method. *Phys Rev B*. 1999;59(3):1758–1775.
33. Perdew JP, Chevary JA, Vosko SH, Jackson KA, Pederson MR, Singh DJ, Fiolhais C. Atoms,molecules, solids, and surfaces-applications of the generalized gradient approximation for exchange and correlation. *Phys Rev B*. 1992;46(11):6671–6687.
34. Dion M, Rydberg H, Schroder E, Langreth DC, Lundqvist BI. Van der Waals density functional for general geometries. *Phys Rev Lett*. 2004;92(24):246401.

35. Gulans A, Puska MJ, Nieminen RM. Linear-scaling self-consistent implementation of the van der Waals density functional. *Phys Rev B*. 2009;79(20):201105.
36. Henkelman G, Jonsson H. A dimer method for finding saddle points on high dimensional potential surfaces using only first derivatives. *J Chem Phys*. 1999;111(15):7010–7022.
37. Henkelman G, Uberuaga BP, Jonsson H. A climbing image nudged elastic band method for finding saddle points and minimum energy paths. *J Chem Phys*. 2000;113(22):9901–9904.
38. Chorkendorff I, Niemantsverdriet JW. *Concepts of Modern Catalysis and Kinetics*. Weinheim: Wiley-VCH, 2003.
39. Vineyard GH. Frequency factors and isotope effects in solid state rate processes. *J Phys Chem Solids*. 1957;3(1–2):121–127.
40. Xu L, Mei D, Henkelman G. Adaptive kinetic Monte Carlo simulation of methanol decomposition on Cu(100). *J Chem Phys*. 2009;131(24):244520.
41. Lyu JH, Wang JG, Lu CS, Ma L, Zhang QF, He XB, Li XN. Size-dependent halogenated nitrobenzene hydrogenation selectivity of Pd nanoparticles. *J Phys Chem C*. 2014;118(5):2594–2601.
42. Liu B, Cheng L, Curtiss L, Greeley J. Effects of van der Waals density functional corrections on trends in furfural adsorption and hydrogenation on close-packed transition metal surfaces. *Surf Sci*. 2014;622:51–59.
43. Crespo-Quesada M, Yarulin A, Jin MS, Xia YN, Kiwi-Minsker L. Structure sensitivity of alkynol hydrogenation on shape- and size-controlled palladium nanocrystals: which sites are most active and selective? *J Am Chem Soc*. 2011;133(32):12787–12794.
44. Ligthart DAJM, van Santen RA, Hensen EJM. Influence of particle size on the activity and stability in steam methane reforming of supported Rh nanoparticles. *J Catal*. 2011;280(2):206–220.

Manuscript received Mar. 5, 2015, and revision received May 27, 2015.